Computers in Biology and Medicine 104 (2019) 70–80

Contents lists available at ScienceDirect

Computers in Biology and Medicine

journal homepage: www.elsevier.com/locate/compbiomed

# A mosaic structure multi-level vascular network design for skull tissue engineering

Jian Qi, Jia Li, Shuxian Zheng*

*Tianjin Key Laboratory of Equipment Design and Manufacturing Technology, School of Mechanical Engineering, Tianjin University, Tianjin, 300354, China*

ARTICLE INFO

*Keywords:*
Tissue engineering
Mosaic structure
Micro-CT
Network topology
Diploic vein
Hard tissues

ABSTRACT

In human skull tissue engineering scaffolds, cell growth and osteogenesis are limited due to the lack of vascular structure. Therefore, a mosaic structure vascular parameterized design method is proposed according to the scanning characteristics of the diploic vein. Using micro-CT scans of skull samples, the features of the diploic vein were extracted, and a multi-level vascular network model was established based on a power diagram. Considering the characteristics of blood flow in the veins, finite element analysis (FEA) of the fluid-solid coupling was established to analyze the effect of blood on vessels with four-level mosaic structures. The results showed that the deformation and stress distribution of vessels were reasonable, and the blood pressure, velocity and shear stress in the designed vascular structure could meet the cell growth requirements. The mosaic structure was prepared by PDMS and cultured in vitro using HUVECs. It was found that most of the cells survived after 48 h, and some cells were attached to the surface mosaic structure. In this method, different levels of vessels nest together, with a curvature that matches the shape of the skull, forming a similar morphology to the native diploic vein, and the local structures can be adjusted flexibly. This mosaic structure vascular design method can be used for network vascular design and experimental studies in hard tissues.

## 1. Introduction

Skull defects are usually caused by open head injury, surgical decompression or diseased skull resection. At present, the skull grafts used for skull repair in clinical are autograft and allograft, while the ideal scaffold material is required to have good biocompatibility, small cytotoxicity, degradability, *etc.*. Bone tissue engineering can fundamentally solve the dysfunction caused by tissue and organ defects by establishing a 3D complex between cells and biological materials.

However, in vitro tissue-engineered skull bones have not been implemented in clinics, it has been found that the supply of oxygen and nutrients to grafts is often limited to 100–200 μm [1] (the diffusion limit of oxygen), preventing the osteoblasts from invading deep inside the scaffold, especially for large-area scaffolds. The main reason was the lack of vascular structure in the scaffold, which result the limitation of oxygen and nutrients. In order for implanted tissue to survive, a vascular network capable of delivering oxygen and nutrients to the cells is needed. In this paper, we proposed a parametric design method to construct bionic vessels based on diploic vein, and intended to apply it in scaffold to accelerate the scaffold vascularization.

Anatomical observations reveal vascular structures in the skull diploë known as diploic veins, as shown in Fig. 1(a) [2]. The structure of the skull can be divided into three layers: the outer and inner plates (compact bones), and the spongy bone (diploë) in the middle. There are vein vessels in diploë, which is called the diploic vein. The diploic veins are large, thin-walled vessels located between the inner and outer plate of the skull. Compared with other veins, the diploic veins have a feature of a flat spatial distribution. To provide adequate nutrients and oxygen for osteoblasts to survive, the scaffold should be designed with vascular structures similar to diploic veins that can better transport nutrients and metabolites [3].

Regarding the vascular design of scaffolds, research has mainly focused on large organs, such as the brain [4] and heart [5]. These vascular design methods can be summarized into two groups: image-based reconstruction and mathematical modeling. 1) Image-based reconstruction includes three procedures: data acquisition, data processing, and model reconstruction. Flasque et al. [4] presented a method for the detection, representation and visualization of the cerebral vascular tree. Bullitt et al. [6] described a method for creating intracerebral vascular trees from vessels segmented based on magnetic resonance angiography (MRA). Image-based reconstruction model has high accuracy, but it has high requirements for data acquisition and model reconstruction. 2) The mathematical modeling method is based on certain conditions, such as the assumption that blood is an

* Corresponding author.
*E-mail addresses:* qijian78@126.com (J. Qi), jli@tju.edu.cn (J. Li), sxzheng@tju.edu.cn (S. Zheng).

https://doi.org/10.1016/j.compbiomed.2018.10.032
Received 20 July 2018; Received in revised form 28 October 2018; Accepted 28 October 2018

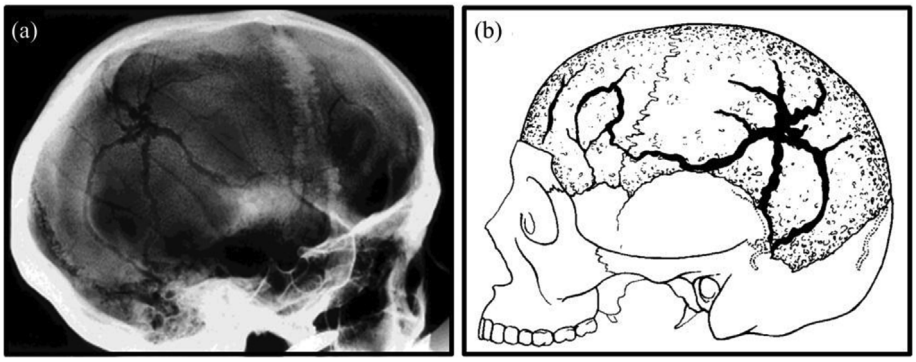


**Fig. 1.** Schematics and lateral x-ray views of diploic vein patterns. (a) Lateral X-ray view of spider-type diploic veins [13]; (b) Schematic diagram of spider-type diploic veins [13].

incompressible Newtonian fluid. Considering the self-similarity of vascular bifurcation structures, these structures could be described via the fractal method [7,8]. Zamir [9] represented the L-system method based on fractal theory. Schreiner [10] and Neumann et al. [11] used the CCO method to construct a 2D arterial tree model, and Karch et al. [12] constructed a 3D arterial tree model using the CCO method. These mathematical methods are generally sensitive to parameters, and if the parameters change, the entire vascular structure might be different, making it difficult to adjust the details. The above modeling methods are aimed at the modeling of blood vessels in soft tissues such as the heart, the vascular design method in hard tissues (such as diploic veins) has not yet been proposed.

With respect to diploic veins, there have been no reports on its vascular design method. Hershkovitz et al. [13] analyzed 141 skull samples and summarized seven types of diploic vein structures, among which the spider type is shown in Fig. 1(a)(b). Rangel et al. [2] used CT to measure diploic veins and concluded that the diameter of the diploic veins was less than 4 mm, with most of these veins presenting a diameter of approximately 1 mm.

The skull scaffold with vascular structures is important for cell growth. In this study, two skull samples were scanned with a micro-CT system. After the feature extraction of diploic veins, a mosaic structure design method was proposed. A fluid-solid coupling finite element analysis (FEA) was employed to verify the design rationality of the vascular structures and parameters. This design method is suitable for designing vascular structures in hard tissues.

## 2. Methods

### 2.1. Diploic vein feature extraction

#### 2.1.1. Sample reconstruction

To obtain accurate features of the diploic veins, two skull samples provided by Tianjin Medical University were scanned. Sample 1 was a piece of skull from the right forehead with a size of 100 mm × 70 mm × 4 mm, and sample 2 was from the occiput with the size of 110 mm × 85 mm × 4 mm, as shown in Fig. 2(a). The samples were scanned with a Nano Vexel 3D X-ray microscope, provided by Sanying Precision Instruments Co., Ltd. The image-scanning resolution was 49.8 μm, and two samples were reconstructed with Avizo software, as shown in Fig. 2(b). From an anatomical perspective, the skull samples were composed of veins, pores and bone trabecular; the vein and pore entities were made visible as shown in Fig. 2(c).

#### 2.1.2. Model preprocessing

To acquire the veins in the diploë, the veins and pores were distinguished by calculating their radius. The preprocessing procedures were as follows: 1) the centerlines of the veins and pores shown in Fig. 2(c) were extracted using Avizo software (an additional file shows this in more detail [see Additional file 1]) the blood vessel extraction process can be seen in Additional file 1). Different radii of the veins and pores were marked with different colors, with red and yellow indicating larger radii, followed by green and blue. Fig. 2(d) shows the centerlines of sample 1 and 2 with partial enlarged details. 2) The proportion of the radius was calculated; the statistical results are shown in Table 1. By comparing the obtained values to radii reported in the literature [2], it can be inferred that blue areas ($r_i < 0.4$ mm, from Table 1) represent pores entities, green areas (0.4 mm $< r_i <$ 0.7 mm, from Table 1) represent small vessels, and red and yellow areas (0.7 mm $< r_i <$ 1.3 mm, from Table 1) represent the main vessels. By filtering the diameter of the vessels, the centerlines of the larger veins, referred to as the main vessels, were extracted from the two samples, as shown in Fig. 2(e).

#### 2.1.3. Vein feature extraction

According to classifications of diploic veins presented in the literature [13], the vascular structures of the two samples can be classified as spider and vine veins. To analyze vascular features, the main vessels were extracted according to vascular connectivity. The feature extraction process included topological feature extraction (the distribution of the vascular network) and local feature extraction (e.g., vascular radius, bifurcation angle). For topological feature extraction, the vein centerline was projected onto a 2D plane and made binary. We found that the main vessel and capillaries presented similar topologies; the main vessels were interwoven with each other and formed vein polygons; small polygons were embedded in large polygons, large polygons were embedded in larger polygons, and so on; and different sizes of vein polygons nested together, forming the diploic vein network, as shown in Fig. 3(a). When the vessels were classified by their radius, the vascular network had the appearance of several levels of vascular structures nested together, as shown in Fig. 3(b). We referred to the closed polygonal regions in a 2D plane as mosaic areas. When it was assumed that the vascular network had 4 levels, the vessels from levels 1 to 3 were referred to as main vessels, and the 4th level was the capillary level. For local feature extraction, the bifurcation angles ($\alpha$) of the veins were analyzed, and it was found that the range of $\alpha$ was approximately 80°~100°. Part of main vessel was selected and crossed with five equidistant planes, and five contour curves were then obtained. We observed that the five contour curves were similar to circles, as shown in the enlarged image in Fig. 3(c), and the radii range ($r_i$) of the circles (vein radius) are provided in Table 1. Through vein feature extraction, the mosaic structure, the bifurcation angles ($\alpha$) and the vein radius ($r_i$) were determined.

### 2.2. Parametric design of blood vessels

The vascular design process based on mosaic structures mainly includes the following procedures: sample data acquisition, 2D mosaic

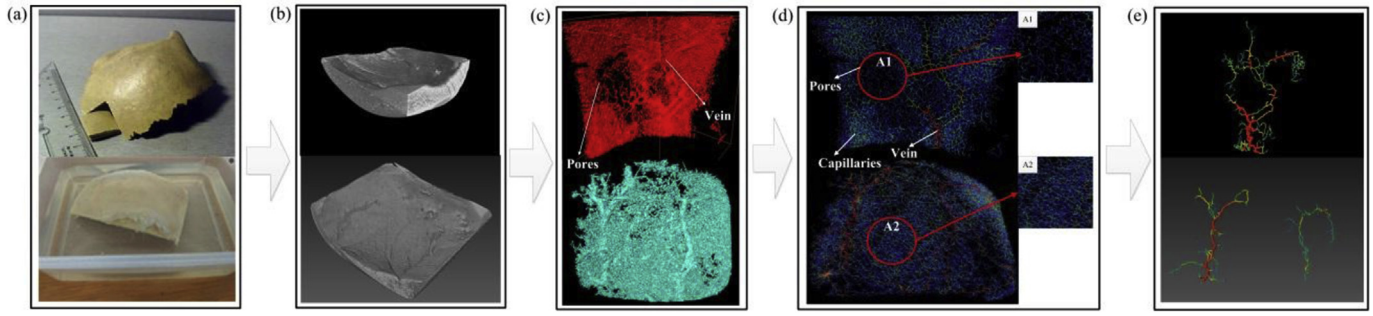


**Fig. 2.** Skull samples and steps of the vascular feature extraction process. (a) The top picture is sample 1, the bottom picture is sample 2, sample 1 is a piece of dry skull from the right forehead with a size of 100 mm × 70 mm × 4 mm and sample 2 is a formalin-soaked piece of skull from the occiput with the size of 110 mm × 85 mm × 4 mm; (b) The 3D models of sample 1 and 2 were reconstructed with Avizo software; (c) The extracted vein and pore entities in two skull samples; (d) The centerlines of sample 1 and 2 with partial enlarged details, different radii of the veins and pores were marked with different colors, red and yellow indicating larger radii, followed by green and blue; (e) The extracted centerlines of large veins from the two samples.

**Table 1**
Statistical results regarding the range and proportion of radii in the skull samples.

| Radius range | Area A1 | Area A2 | Larger radius area |
|---|---|---|---|
| $r_i < 0.4$ mm | 95% | 91% | 63% |
| 0.4 mm $< r_i <$ 0.7 mm | 5% | 9% | 23% |
| 0.7 mm $< r_i <$ 1.3 mm | 0 | 0 | 14% |

topology generation, 3D centerline generation and vascular model design, as shown in Fig. 4.

### 2.2.1. Parameterized definition of mosaic structure

The diploic vein network was composed of different levels of mosaic structures. As the mosaic area ($S$) can be parameterized controlled, the structures of vascular network can be determined. A power diagram [14] can generate circles with controllable areas in a plane and was used here to design the mosaic structures of different sizes and locations.

The power diagram is an extension of the Voronoi diagram [14]: let $S = \{p_1,p_2,\ldots,p_n\}$ be a set of points in 2D continental space, and add weight $w_i (i = 1,2,\ldots,n)$ for each generator $p_i$. $\mathrm{Vor}(p,d_{pw}) = \mathrm{Vor}_{pw} = \{V(p_i),\ldots,V(p_n)\}$defined by the power distance

$$d_w(p, p_i) = \|p - p_i\| - w_i \quad (1)$$

is referred to as the weighted power diagram generated by set $S$, and set $V(p_i)$ is referred to as the power polygon associated with $p_i$. The generator $p_i$ is determined by the approximate center point of the mosaic area, the weight $w_i$ is related to the area of the mosaic area, set the area of a circle equivalent to the area of the mosaic area, then the radius $r$ of the circle is the weight $w_i$ of the corresponding generator $p_i$.

Fig. 5(a) shows the power diagram in a 2D plane, where the black dots represent the generator ($p_i$), and the blue lines represent the power edges. The power edges were connected to each other to form a network structure, which was similar to the mosaic areas projected from the skeleton of the diploic vein. $S$ can be calculated by the number of pixels in the mosaic area, and different areas are distinguished by different colors, as shown in Fig. 5(b). $S$ and the occupation ratio ($t_p$) of sample 1 were shown in Table 2, which can be employed to control the size and location of the generators in the vascular design process. The area of the control circle ($S_c$) can be set to equal to $S$, and the number of control circles ($c_p$) was determined by the following equation:

$$c_p = \frac{S_a \cdot t_p}{S_c} \quad (2)$$

Based on the statistics shown in Table 2 and formula (2), the number and size of $c_p$ were determined, and the corresponding power diagram was then produced, consisting of the mosaic areas. The boundaries of the mosaic areas were the centerlines of the vessels. For example, in vessels with two levels of mosaic areas, the first-level control circles and power diagram (blue lines) were generated with reference to formula (2). Then the control circles were located uniformly in every first-level mosaic area, resulting in the 2nd level power diagram (brown lines). To avoid interference between vessels, nodes that were too close together (node distance of less than 1.2 times the diameter of vessel) were removed, and a 2D line model of vessels with two levels was achieved, as shown in Fig. 5 (c).

### 2.2.2. Parameterized definition of the centerline model

After the mosaic polygons were generated using the power diagram, it was necessary to convert the 2D line model to the 3D centerline model, and determine the vascular path for the sweeping procedure.

1) 3D mosaic structure generation

The transition of the mosaic topology from 2D to 3D can be achieved via the hierarchical approach. First, the plane center point ($O_c$) was found, and $n_c$ equidistant concentric circles to point $O_c$ were

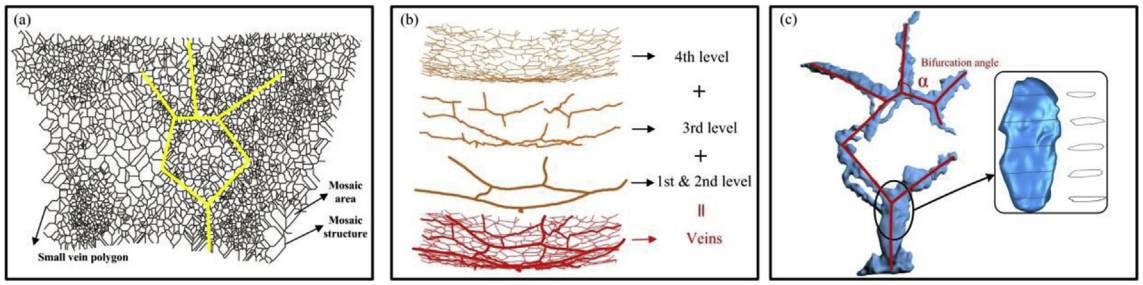


**Fig. 3.** Centerlines of diploic veins and main vessel of sample 1. (a) Binarized centerline graph of vascular network; (b) Schematic diagram of vascular network composed of several levels of mosaic structures; (c) The extracted main vessel of sample 1 with details of bifurcation angles ($\alpha$) and the vein radius ($r_i$).

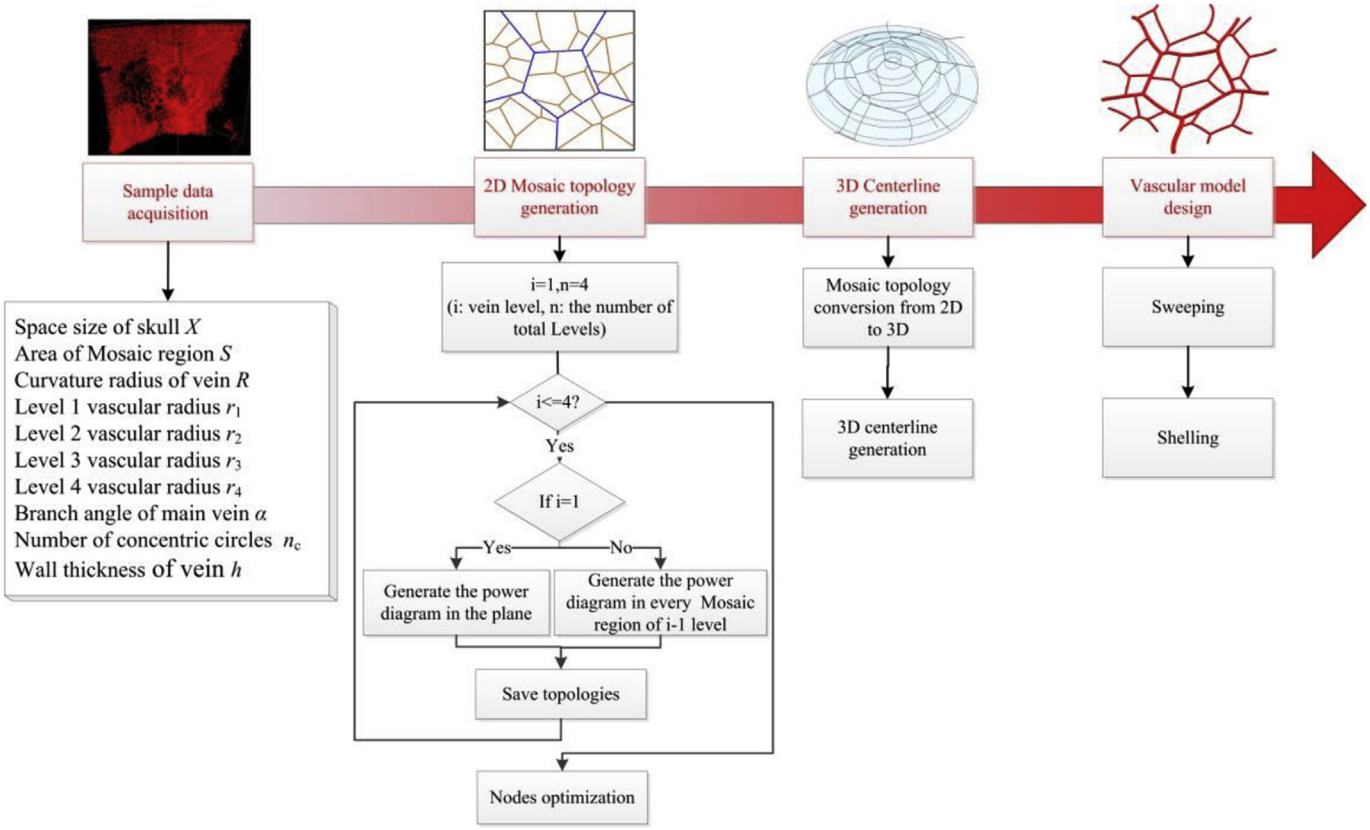


**Fig. 4.** Flow chart of vascular design with 4-level mosaic structures.

then drawn, which were offset at the $Z$ axis, as shown in Fig. 6(a). The larger the value of $n_c$, the smoother the vascular bending will be. According to the spatial bending curvature ($R_c$) of the skull sample, the max offset distance ($z_c$) could be calculated using formula (3). The plane area was assumed to be $L \times L$, and the max offset distance was then calculated using the following formula:

$$z_c = \frac{R_c - \sqrt{R_c^2 - \frac{1}{4}L^2}}{n_c} \tag{3}$$

where the nodes belonging to the smallest concentric circle were assigned random $Z$ coordinates in [0, $z_c$], and the nodes belonging to larger circles were assigned $Z$ coordinates in [$z_c$, $2 \times z_c$], [$z_c$, $3 \times z_c$]…

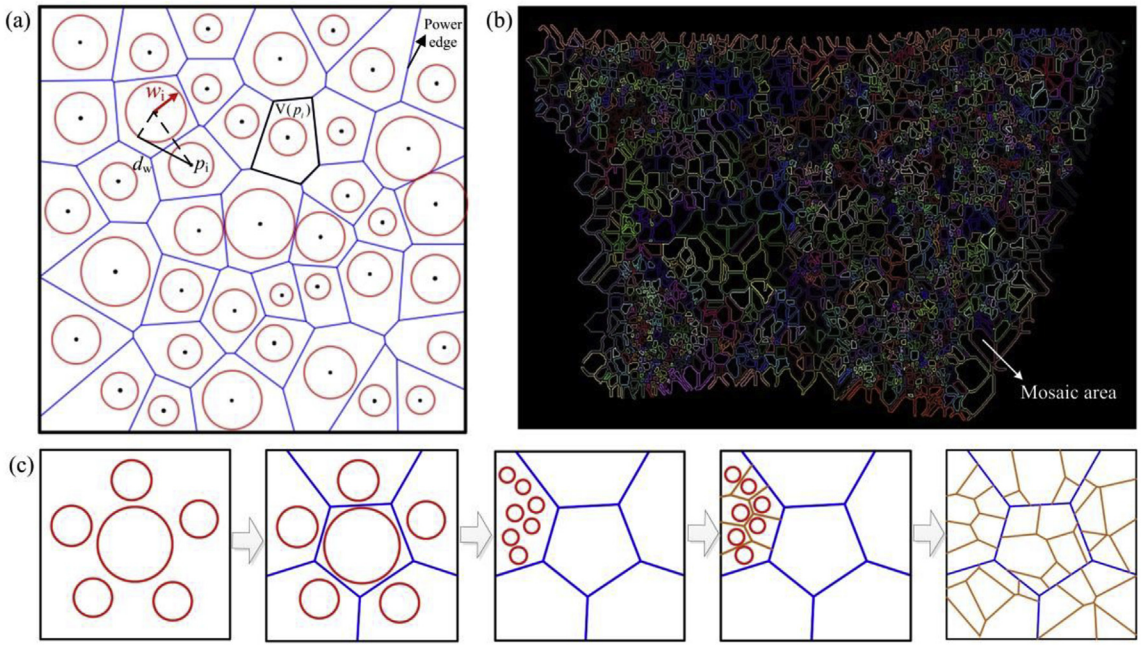


**Fig. 5.** Power diagram and design process of mosaic structure. (a) Schematic of 2D power diagram; (b) Different size mosaic areas marked with different colors in sample 1; (c) Schematic of the 2-level mosaic structure design.

**Table 2**
Statistics for the range of mosaic areas in sample 1.

| Range of mosaic areas, $S$(mm$^2$) | Occupation ratio $t_p$ |
|---|---|
| 0.3–7 | 68% |
| 7–79 | 17% |
| 79–314 | 12% |
| 314–1256 | 3% |

**Table 3**
Vascular path generation.

| Vascular segment | Path of 1st-level vessels | Path of 2nd-level vessels |
|---|---|---|
| 1 | $N_{b1}\rightarrow N_{b2}\rightarrow N_{b9}\rightarrow N_{b7}\rightarrow N_{b8}$ | $N_{s5}\rightarrow N_{s6}\rightarrow N_{s8}\rightarrow N_{s9}$ |
| 2 | $N_{b2}\rightarrow N_{b3}\rightarrow N_{b5}\rightarrow N_{b6}$ | $N_{s4}\rightarrow N_{s2}\rightarrow N_{s1}$ |
| 3 | $N_{b9}\rightarrow N_{b10}$ | $N_{s7}\rightarrow N_{s6}$ |
| 4 | $N_{b7}\rightarrow N_{b5}$ | $N_{s3}\rightarrow N_{s2}$ |
| 5 | $N_{b3}\rightarrow N_{b4}$ | $N_{s10}\rightarrow N_{s8}$ |

$[z_c, n_c \times z_c]$. Additionally, the nodes that exhibited the same *X, Y* coordinates also presented the same *Z* coordinates to guarantee that the centerline segments were connected to each other, then the transformation of the mosaic structure from 2D to 3D was completed.

2) Vascular path definition

After the 2D line (Fig. 5(c)) to the 3D centerline model (Fig. 6(a)), the vascular paths need to be determined for sweeping procedure. Two-level vessels were used to illustrate vascular path generation. In the case of Fig. 6(b), the red and pink lines indicate the mosaic structures of the 1st- and 2nd-level vessels; the red and pink arrows indicate the direction of blood flow of the 1st- and 2nd-level vessels; and ($N_{b1}$…$N_{b10}$) and ($N_{s1}$…$N_{s10}$) are the nodes of the 1st- and 2nd-level vessels, respectively.

First, the 1st-level vascular path was generated, and the nodes of the 1st level were filtered out, as shown in red in Fig. 6(b). Node $N_{b1}$ was set as the starting point; the 1st-level vector ($v_{c1}$) was set up vertically; and $v_{c1}$ was then employed to screen the nodes, which also represented the direction of blood flow in the 1st-level vessel. Then, the connected node (such as $N_{b9}$ or $N_{b3}$ connected with $N_{b2}$) with a minimum angle (such as 52° in Fig. 6(b)) of $v_{c1}$ was selected as the next node until the end node. The rest of the centerlines could be generated in the same way, until all nodes in the 1st level were allocated.

Second, the vascular path of the 2nd level was generated. The vessel nodes of level 2 were filtered out, as shown in pink in Fig. 6(b). The nodes (such as $N_{s5}$) on the 1st-level vessels were set as starting points; the vector perpendicular to the main vessel was set as the 2nd-level vector ($v_{c2}$, pink vector); and the connected node with a minimum angle of $v_2$ was then selected as the next node, until all nodes were allocated. Table 3 shows the vascular path generation process.

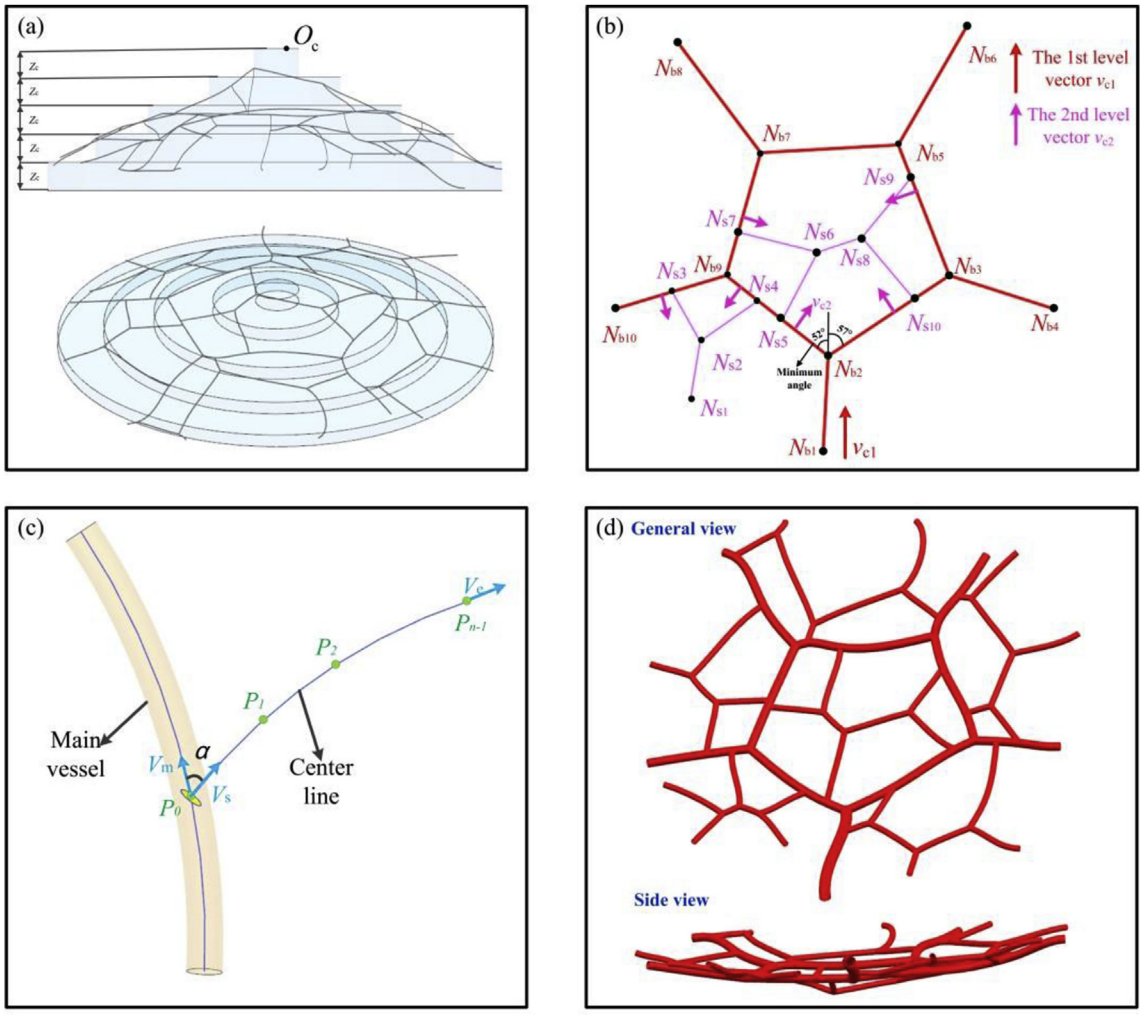


**Fig. 6.** (a) Schematic diagram mosaic structure transition from 2D to 3D; (b) Schematic diagram of vascular path generation; (c) Centerline-parameterized model constructed by using B-Spline curves; (d) Different views of vascular models after sweeping and shelling operations.

*2.2.3. Parameterized definition of surface sweeping*

Current 3D mosaic structures are fold lines, which can be curve fitted using a B-spline curve. $V_s$ was set as the tangent vector of the starting point ($P_0$) of the centerline; $V_e$ was set as the tangent vector of the end point ($P_{n-1}$) of the centerline; and $V_m$ was set as the direction of blood flow in the main vessel. If $P_0$ was located on the main vessel, $V_s$ and $V_m$ were set to angle $\alpha$; otherwise, $V_s$ was determined by the first two nodes ($P_0$, $P_1$) of the centerline. $V_e$ could be determined via the same method. Using nodes as the data points, the tangent vectors $V_s$ and $V_e$ were combined, and it was ensured that the curves at the knot met the second order of continuous conditions. Then, the 3D centerline model was obtained by employing the cubic B-spline curve, as shown in Fig. 6(c).

Using the 3D centerline model combined with vascular cross-section features, the vascular model could be built after sweeping and shelling operations. The radius of all levels of vessels could be determined based on the statistical data in Table 1. The sweep cross-section was generated at the starting point, and sweeps were performed along the centerlines of the vessels of each level, after which swept surfaces with different radii were formed, as shown in Fig. 6(d).

## 3. Results

### 3.1. Case study

As described above, the vascular radius ($r_i$), bifurcation angle of vessels ($\alpha$), and mosaic area ($S$) were counted out. The space size of skull $X$ and the curvature radius of vessel $R$ could be measured directly based on the skull defect; *e.g.,* the size of $X$ was approximately 100 mm × 100 mm × 3 mm, and $R$ was 125 mm. For wall thickness $h$, the ratio of vessel wall thickness to the diameter of the vessel was the relative wall thickness [15], which satisfies

$$\frac{h}{2r} = 0.04 \sim 0.1 \tag{4}$$

where $r$ is the radius of the vessel. Then, the design parameters of all levels vessels could be expressed as $VM(X, S, R, r_1, r_2, r_3, r_4, \alpha, n_c, h)$.

Using the mosaic structure method, the spider and vine vessels (described in Ref. [13]) could be designed. To verify the feasibility of this method, three different forms of vascular cases were constructed with space $X$ = 100 mm × 100 mm × 3 mm.

**Case 1.** A spider-type structure of vessel was designed. The design parameters according to previous statistics are shown in Table 4, and the vascular structure with 4 levels is shown in Fig. 7(a). The volume of the main vessel was 1074 $mm^3$; the total volume of vessel was 2877 $mm^3$; and the vascular density in space $X$ was 9.6%. It can be seen that the vessels are uniformly distributed in space with multiple levels, and the vascular structure shows the same concave characteristic as diploic veins.

**Case 2.** To show the effects of the mosaic areas on the vascular morphology, $S$ was reduced to 8 $mm^2$-1256 $mm^2$, while the other parameters remained the same as in Case 1. The design result was shown in Fig. 7(b). The total volume of vessels in Case 2 was 4270 $mm^3$, and the vascular density in space $X$ was 14.2%.

**Case 3.** A vine-type vessel was designed. By intercepting the 3D centerline model of Case 1, the vine-type vessel could be generated after the sweeping and shelling operations, as shown in Fig. 7(c). From the above three cases, it can be seen that 2 types of vascular structures can be designed by adjusting the design parameters, indicating that the mosaic structure method applies to different types of vascular design.

**Table 4**
Design parameters of Case 1.

| Name | Size | units |
|---|---|---|
| Space size of skull $X$ | 100 × 100 × 3 | mm |
| mosaic area $S$ | 11–1256 | $mm^2$ |
| Curvature radius of vessel $R$ | 125 | mm |
| Level 1 vascular radius $r_1$ | 1.3 | mm |
| Level 2 vascular radius $r_2$ | 1.0 | mm |
| Level 3 vascular radius $r_3$ | 0.7 | mm |
| Level 4 vascular radius $r_4$ | 0.4 | mm |
| Bifurcation angle of vessels $\alpha$ | 30–60 | ° |
| Number of concentric circles $n_c$ | 12 | |
| Wall thickness of vessel $h$ | 0.1 | mm |

### 3.2. Mosaic structure analysis

The design method forms a spatial vascular network through multiple layers of mosaic structures. In the process of blood vessel parameterization design, the space size of skull $X$, the curvature radius of vessels $R$ were determined by the defective skull; the wall thickness of vessel $h$ was determined with reference to similar blood vessels; the number of concentric circles $n_c$ could change the spatial curvature degree of the vascular network, and had little effect on the topology of blood vessels; the bifurcation angle of vessels $\alpha$ only affected the initial tangent of the vascular centerline, and had little effect on the vascular topology; the mosaic area $S$ and vascular radius $r_i$ had effect on blood vessel density and topologies. The vascular radius $r_i$ is related to the mosaic area $S$, and the vascular radius $r_i$ decreases as the mosaic area $S$ decreases. Therefore, here we mainly study the effect of mosaic area on vascular structure.

By changing the size of mosaic area, the vascular density can be adjusted. The mosaic areas were taken as a key factor to analyze the effect on the volume, surface area, length, vascular segment count and vascular density of blood vessels by changing its size.

Regarding the statistical data of mosaic area in Table 2, the mosaic area of 0.3–79 $mm^2$ accounts for 85%, so we set the average mosaic area to be 0.3–79 $mm^2$. The number of control circles in this range was set to be 5, 10, 20, 40, 80, corresponding to the average mosaic area of blood vessel models were 87 $mm^2$, 74 $mm^2$, 41 $mm^2$, 28 $mm^2$, 12 $mm^2$ from left to right in Fig. 8. Then the total volume, total surface area, total length of blood vessels, vascular segments count and vascular density were calculated as shown in Fig. 8. It can be seen that with the decrease of average mosaic area, the total volume, total surface area, total length of blood vessels, vascular segment count and vascular density increased, especially the blood vessel segment count, meaning a large increase in small blood vessels. The increase in the volume, surface area, and vascular density are conducive to improving the exchange efficiency of oxygen and nutrients between cells.

In the process of blood vessel design, blood vessel density can be adjusted according to clinical needs by adjusting the size of the mosaic area. Increasing the number of blood vessel levels and reducing the mosaic area can construct a dense vascular network, but what needs attention is the excessively small blood vessel diameter and dense blood vessel structure will pose a challenge to the blood vessel manufacturing process.

### 3.3. Finite element analysis

To verify the reliability of the design method, the 1st-to 3rd-level vessels in Case 1 were analyzed using Ansys Workbench. As the effect of vessel deformation on blood flow was relatively small, the following fluid-structure one-way coupling analysis was used to analyze the stress and blood flow effects.

Assuming that blood is an incompressible Newtonian viscous fluid, the density of blood was set to $\rho_b$ = 1050 kg/$m^3$, the viscosity coefficient was $\eta_b$ = 0.0035kg/($m^2$·s), the elastic modulus $E_v$ = 110 MPa, Poisson's ratio $\mu_v$ = 0.45, density $\rho_b$ = 1150 kg/$m^3$ [16,17]. The tetrahedral meshes were used to divide the blood and vascular geometric models, which contain 1,418,818 and 110,146 elements, as shown in

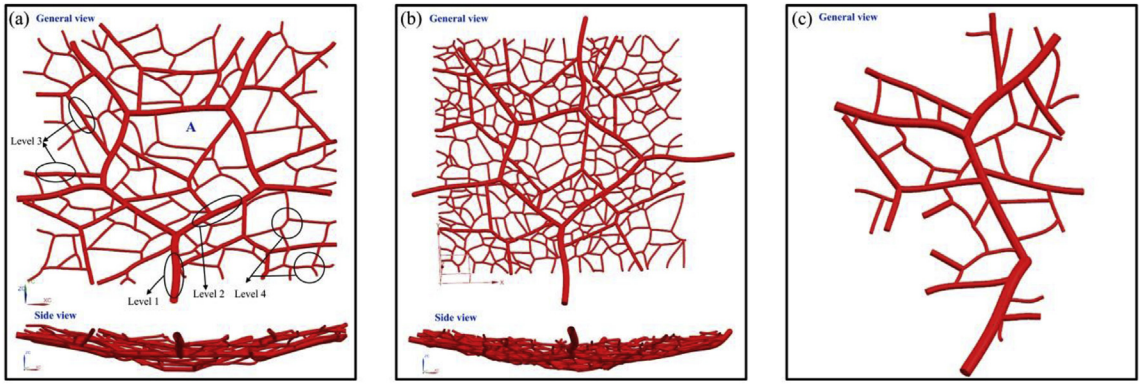


**Fig. 7.** Vascular models of mosaic structure with different design parameters. (a) Vascular model of Case 1; (b) Vascular model of Case 2; (c) Vascular model of Case 3.

Fig. 10(e).

In the statics analysis of vessels, fixed constraints were added at the inlet and outlets, as shown in Fig. 10(a). In a smooth tube, the Reynolds number (*Re*) determines whether the flow state is laminar or turbulent:

$$\mathrm{Re} = \rho v r/\eta \tag{5}$$

where ρ is the blood density; $v$ is the flow rate; $r$ is the blood vessel radius; and $\eta$ is the blood viscosity. According to formula (5), the calculation shows that $Re < 1000$, so the blood flow in the vessel was calculated as a laminar flow. The inlet and outlets were set as fixed constraints, and the pressure of the blood flow in the fluid simulation was then applied to the vascular wall to calculate its deformation and stress.

In order to find the suitable perfusion parameters in vitro, the inlets velocity of the 1st-level of the vessel were set to $v_{in}$ = 0.4 m/s, 4 m/s, 7 m/s [18], and the outlets pressure were set to $P_{out}$ = 660Pa, 9660Pa, 18600Pa [18], as shown in Table A1(Additional file 1). The FEA method was used to analyze the average shear stress, mean pressure of the vessel wall and maximum blood velocity with different inlet velocity and outlet pressures. The residual and blood vessel outlet flow were monitored, and when the residual was less than 0.001 or the blood vessel outlet flow was stabilized, then the analysis was considered to converge. Fig. 9 shows the effect of inlet velocity and outlet pressure on average shear stress, average pressure, and maximum velocity of blood vessels.

It can be seen from Fig. 9 that the average shear stress is very sensitive to the blood flow velocity $v_{in}$. As $v_{in}$ increases, the average shear stress increases multiplied; there is no significant relationship with blood pressure. The average pressure is positively correlated with the outlet pressure, and the pressure gradually decreases from the inlet to the outlet of blood vessels, so the average pressure is greater than the outlet pressure. The maximum blood flow velocity generally occurs in

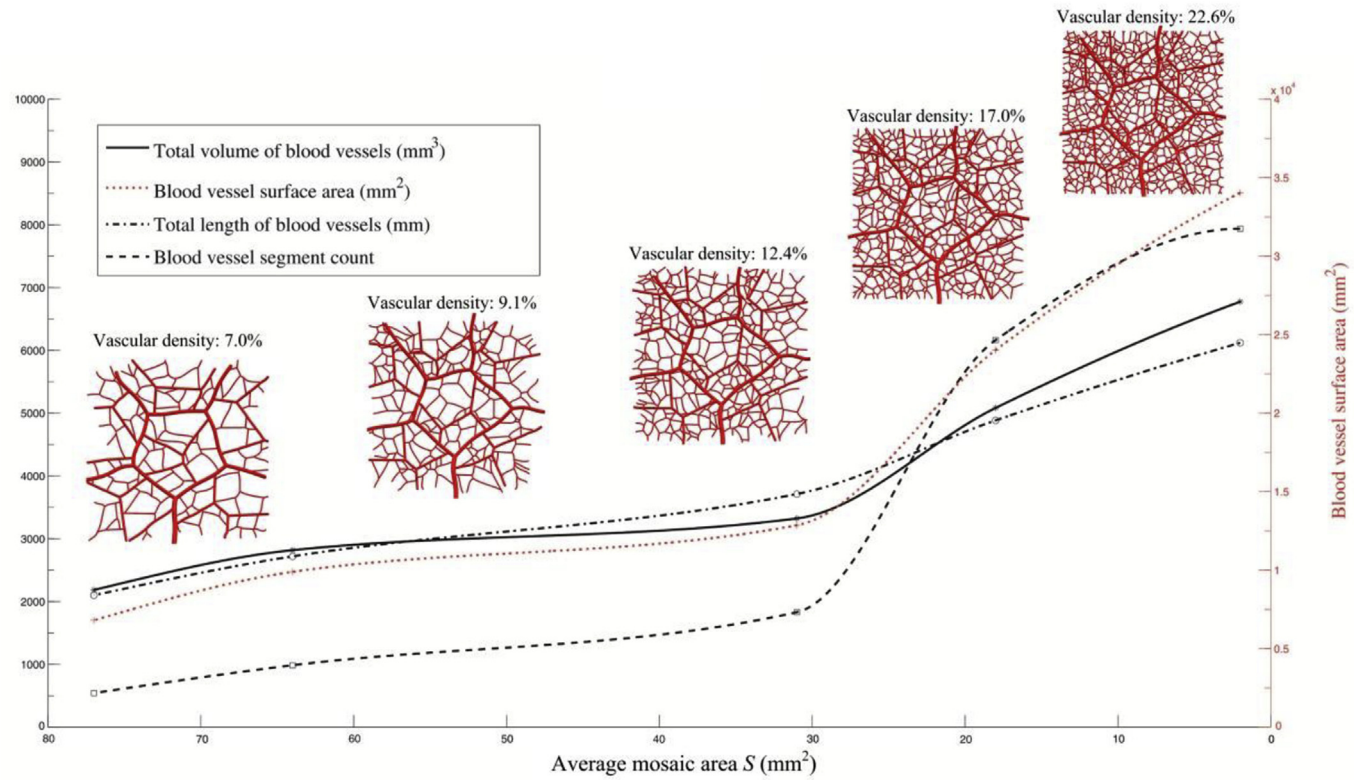


**Fig. 8.** The average mosaic areas of the blood vessel model in Fig. 8 were 77 mm², 64 mm², 31 mm², 18 mm², 2 mm² from left to right, respectively. The graph shows the relationship between the average mosaic area and total volume (total surface area, total length, vascular segment count and vascular density) of blood vessels.

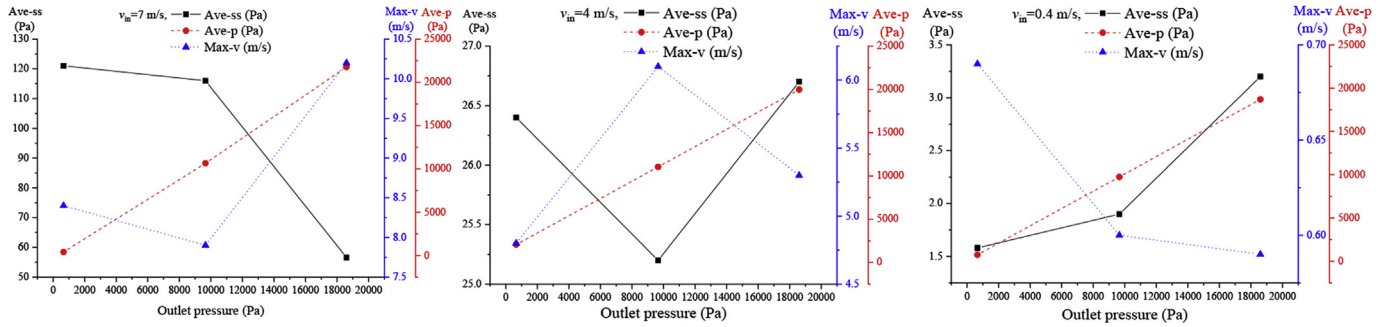


**Fig. 9.** (a) when $v_{in}$ is 7 m/s, the relationship between Ave-ss, Ave-p, Max-v and Oulet pressure; (b) when $v_{in}$ is 4 m/s, the relationship between Ave-ss, Ave-p, Max-v and Oulet pressure; (c) when $v_{in}$ is 0.4 m/s, the relationship between Ave-ss, Ave-p, Max-v and Oulet pressure.

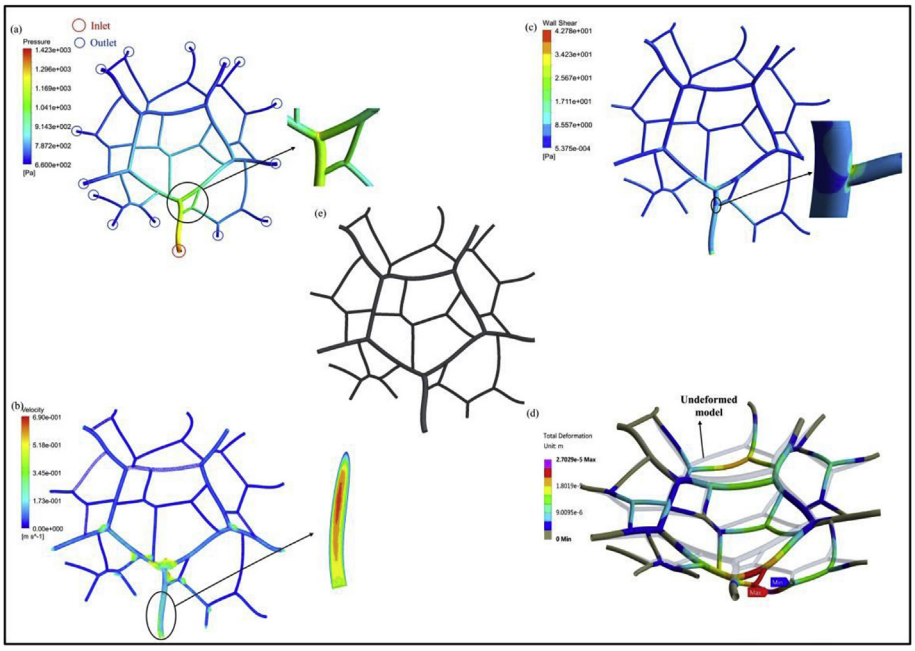


**Fig. 10.** FEA results of designed mosaic vascular structure and branches. (a) Blood pressure on the vessel wall of mosaic vascular structure (level 1–3); (b) Velocity vector diagram of mosaic vascular structure (level 1–3); (c) Shear stress on the vessel wall of mosaic vascular structure (level 1–3); (d) Deformation of the mosaic vascular structure (level 1–3); (e) Meshing of blood model.

the main blood vessel, which is greater than the inlet blood flow velocity, as shown in Fig. 10(a). For endothelial cells, appropriate shear stress (0–3Pa [19]) can promote endothelial cell proliferation. Therefore, the 7th group of experiments in Table A1 was selected as an in vitro perfusion parameter for endothelial cells.

The analysis results of the 7th group in Table A1 were shown in Fig. 10. The distribution of blood pressure on the vessel wall is shown in Fig. 10(a). The average pressure in the whole structure was approximately 750 Pa, the maximum pressure at the inlet was 1423 Pa. Fig. 10(b) is the velocity vector diagram. The velocity at the inlet was relatively high, and the maximum velocity, 0.69 m/s, was located at the bifurcation of the main vessels. With the blood flow to different branches, the flow rate gradually slows down. The inlet of the vessel was cut along the central plane to observe the velocity distribution, as shown in the partial magnification diagram in Fig. 10(b). It can be seen that the maximum velocity of the blood flow was 0.65 m/s, which occurred at the center of the central plane. The distribution of shear stress on the vessel wall is shown in Fig. 10(c). The average shear stress was 1.58 Pa. The maximum shear stress occurred at the branch of the main vessel due to the large flow rate of blood. The vascular deformation is shown in Fig. 10(d). With the vascular structure distributed in a concave space, the effect of blood flow increases the structural bending. While the bending deformation was not large, the maximum deformation was 0.027 mm, located on the right branch of the main vessel.

### 3.4. Vascular fabrication

Taking a planar mosaic vascular structure as an example, it was fabricated by Polydimethylsiloxane (PDMS) using mold forming [20]. First, the upper and lower molds of the mosaic structure were prepared by 3D printing, as shown in the Fig. 11(a). Then the PDMS scaffold was prepared by mixing Sylgard 184 (Dow Corning) in 10:1 base to curing agent ratio. After the PDMS scaffold was cured at 65 °C for 4 h, the fabricated blood vessel was obtained, as shown in Fig. 11(b).

### 3.5. Cell culture

The blood vessels play the role of oxygen and material transport in scaffold. To test the cell morphology in blood vessels, human umbilical vein endothelial cells (HUVECs) were cultured static in vitro, the culture medium composed of DMEM(Thermo,C11885), 10%FBS (Gibico,10099), 1%L-glutamine(Thermo, 25030081), 1% Pen/strep (Thermo, 15140122). The cell density was adjusted to $5 \times 10^5$/ml, and the cell suspension was injected into the blood vessels in scaffold. After being placed in the incubator for 1 h, the scaffold was added culture medium for further 48 h. Then the scaffold was performed fluorescent staining (Live/Dead™ Viability/Cytotoxicity Kit, for mammalian cells (Invitrogen, L3224)), 4 bifurcation nodes were selected for observation under inverted fluorescence microscope, as shown in Fig. 11(a). The partial enlargement photographs of ① to ④ can be referred to

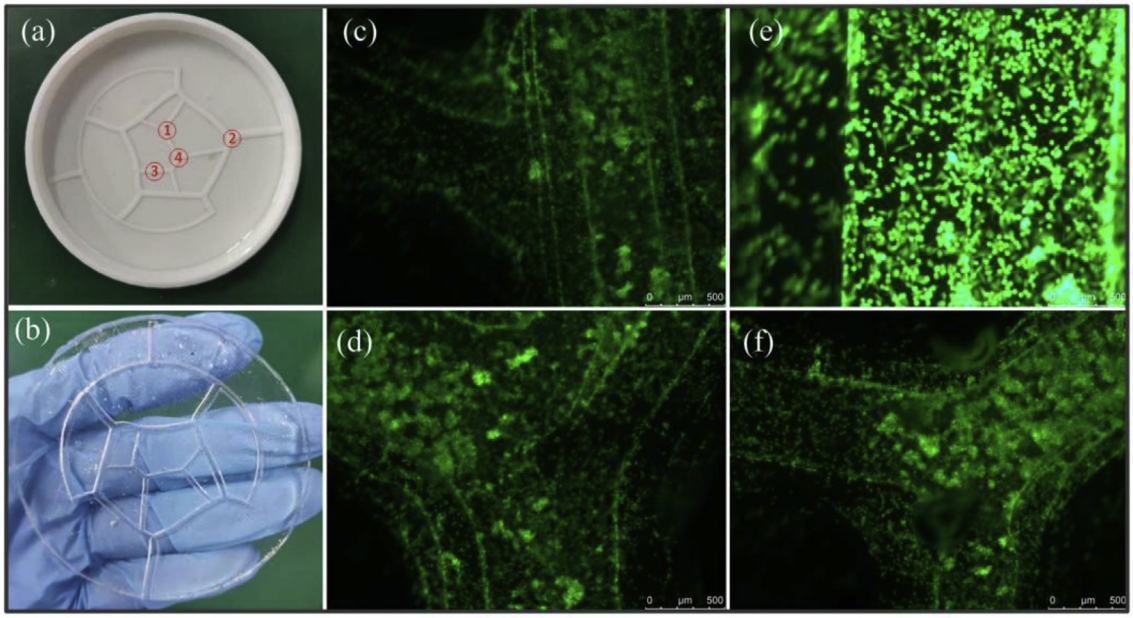


**Fig. 11.** Scaffold fabrication process and distribution of HUVECs in the scaffold. (a) Vascular fabrication mold, ① to ④ were 4 bifurcation nodes for observation; (b) PDMS vascular structure; (c)–(f) Partial enlargement photographs of live-dead fluorescent staining of HUVECs taken under an inverted microscope, corresponding to ① to ④ nodes respectively.

Fig. 11(c–f) respectively. It was found the HUVECs can proliferate in the blood vessels.

## 4. Discussion

### 4.1. Structural design

In vascular design studies, vessels are commonly represented as binary tree structures [21–23], as shown in Fig. 12. Compared to the common used bifurcated blood vessels [9–12], mosaic structure vessels ensures smooth blood flow and minimizes the effects of thrombosis. If the vascular blockage occurs in the parent node of bifurcated blood vessels, the posterior blood vessel branches will be affected, as shown in Fig. 12(a–c), which can cause a large area of cell hypoxia and death easily. However, if blockage occurred in mosaic structures, blood can flow through the bypass, which is a great significance for large area tissue culture in vitro. Besides, for skull blood vessels, due to the location and topology of diploic veins, it is more reasonable to design a network structure of vessels.

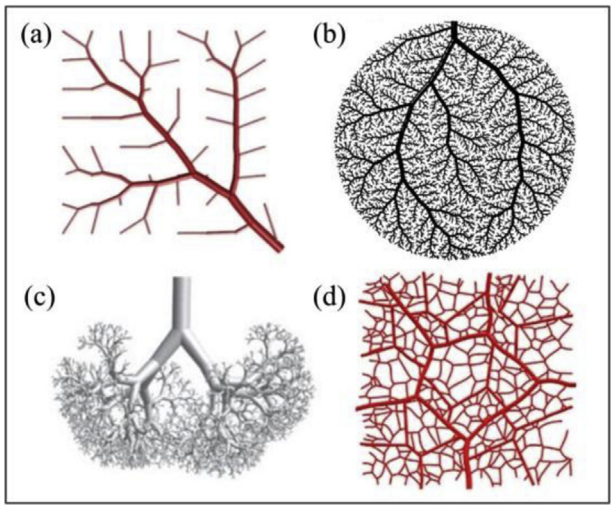


**Fig. 12.** (a) Artery structures generated by annealing approach [21]; (b) Mathematical model of blood vessels [22]; (c) Design of vascular networks: A mathematical model approach [23]; (d) Diploic vein generated by mosaic structure design method.

In addition, compare to soft tissue, such as heart [24], the extraction and design of diploic veins in skull have the following two characteristics:

1) Diploic vein can be extracted by hard tissue structures. Due to the diploic veins locate in the middle of the two layers of hard tissues, its space structure is limited to a spatial curved plate-like shape, which restrain the distribution of the diploic veins in the interior. The morphological of diploic vein therein can be extracted through the constraints of the hard tissues. In soft tissues, the distribution of blood vessels tends to be evenly distributed [21–23], as shown in Fig. 12(a–c). However, in some specific areas of the skull, there is only a small distribution of blood vessels, then in the mosaic structure, by controlling the number and locations of the control circles, the number of vessels can be reduced like the area A in Fig. 7(a).
2) Small blood vessels and pores were mixed together. From Fig. 2(c) and Table 1, it can be seen that the small blood vessels and pores have similar dimension and topology with radius of 0.7 mm or less [2]. Due to the scanning resolution, it was difficult to distinguish small blood vessels and pores in hard tissues. However, by analyzing the topologies of small blood vessels, we found that it has similar topological characteristics with large blood vessels, and then the nested design principle of multi-level blood vessels was proposed.

### 4.2. Finite element analysis

To test the rationality of the mosaic structure design method, blood vessels in Case 1 were analyzed by FEA. The results showed that the distribution of pressure (average 750 Pa) and shear stress (average 1.58 Pa) on the vessel wall are uniform for endothelial cells. As it is suitable to have a pressure range of 267 Pa–18620 Pa [25] and a shear stress range of 0–2 Pa [19], the designed vascular structures meet the growth requirements of endothelial cells in ideal conditions. Since the diploic veins are close to the diploë, the impact of blood flow on vessels

is small. With the fixed constraints on the ends (inlet and outlets) of vessels, the analysis shows that the maximum deformation of vessels is 0.027 mm, which can be ignored, proving that the fluid-solid coupling analysis is reasonable (the comparative analysis between bifurcation and mosaic vascular structures can be referred to Additional file 1).

### 4.3. Vascular fabrication and cell culture

The mold forming method we used to prepare vascular structures has the characteristics of easy made, low cost, compared to coaxial extrusion [26], sacrificial material [27], direct deposition method [28]. After the vascular structure fabricated, the HUVECs were implanted into it. By culturing HUVECs for 48 h in vitro, it was found that HUVECs were alive, and uniformly distributed on various vascular structures. Cell agglomeration could be seen on small vessels, and some cells could attach to the vessel wall. Material exchange efficiency is usually one of the limiting factors that affect cell viability. The exchange of oxygen and metabolic wastes is usually transported by passive diffusion [29,30], which requires that the blood circulation system be close enough to the cells for maximum exchange efficiency. Mosaic structure vascular network with multi-level diameters promote the distribution of oxygen and nutrients and reduce the diffusion distance from blood vessels to cells [31–33].

### 4.4. Future work

It needs to be pointed out that the scanning resolution of micro-CT affects the model reconstruction quality. Due to the large size of the scanned skull, the resolution of the micro-CT was set to 49.8 μm to avoid huge data. The small vessels and pores with a radius of less than 400 μm will be hard to distinguish between data processing. The scanning resolution can be appropriately increased when scanning bone samples. Researchers need to find a balance between scanning resolution and data volume. In the following work, we are going to use dynamic perfusion to study the proliferation and differentiation of HUVECs and promote their formation of vascular structures [34,35].

## 5. Conclusion

For the vascularization of a tissue engineered skull scaffold, a mosaic structure design method is proposed based on the natural diploic vein, which can be used to design the vascular structure in hard tissue quickly and flexibly, meeting the requirements of different scales of the scaffold. By adjusting the design parameters, this method can be used to design a variety of vascular morphologies, such as spider and vine vessels. After structure analysis and cell culture, it was found that mosaic structure vessels could meet the requirements of cell growth, which verified by cell culture experiments in vitro. This mosaic structure design method offers a new approach to vasculature design in tissue engineering, especially for net-kind vascular structures in hard tissues.

## Contributions

J.Q.,S.Z. conceived of the study, S.Z.,J.L. helped with the revision of the manuscript, all authors read and approved the final manuscript.

## Competing interests

The authors declare no competing interests.

## Acknowledgement

This work was supported by the National Natural Science Foundation of China (51575380 and 51375335).

## Appendix A. Supplementary data

Supplementary data to this article can be found online at https://doi.org/10.1016/j.compbiomed.2018.10.032.

## References

[1] R.E. Horch, et al., Cancer research by means of tissue engineering–is there a rationale? J. Cell Mol. Med. 17 (2013) 1197–1206.
[2] G. Rangel de Lázaro, J.M. de la Cuétara, H. Píšová, C. Lorenzo, E. Bruner, Diploic vessels and computed tomography: segmentation and comparison in modern humans and fossil hominids, Am. J. Phys. Anthropol. 159 (2016) 313–324.
[3] A.K. Ekaputra, G.D. Prestwich, S.M. Cool, D.W. Hutmacher, The three-dimensional vascularization of growth factor-releasing hybrid scaffold of poly (ε-caprolactone)/collagen fibers and hyaluronic acid hydrogel, Biomaterials 32 (2011) 8108–8117.
[4] N. Flasque, M. Desvignes, J.-M. Constans, M. Revenu, Acquisition, segmentation and tracking of the cerebral vascular tree on 3D magnetic resonance angiography images, Med. Image Anal. 5 (2011) 173–183.
[5] J. Lee, P. Beighley, E. Ritman, N. Smith, Automatic segmentation of 3D micro-CT coronary vascular images, Med. Image Anal. 11 (2007) 630–647, https://doi.org/10.1016/j.media.
[6] E. Bullitt, et al., Symbolic description of intracerebral vessels segmented from magnetic resonance angiograms and evaluation by comparison with X-ray angiograms, Med. Image Anal. 5 (2001) 157–169.
[7] A. Kamiya, T. Takahashi, Quantitative assessments of morphological and functional properties of biological trees based on their fractal nature, J. Appl. Physiol. 102 (2007) 2315–2323.
[8] G. Finet, et al., Fractal geometry of arterial coronary bifurcations: a quantitative coronary angiography and intravascular ultrasound analysis, J. EuroPCR. 3 (2008) 490–498.
[9] M. Zamir, Arterial branching within the confines of fractal L-system formalism, J. Gen. Physiol. 118 (2001) 267–275.
[10] W. Schreiner, Computer generation of complex arterial tree models, J. Biomed. Eng. 15 (1993) 148–150.
[11] W.S.M.N. Friederike Neumann, Computer simulation of coronary arterial trees, Adv. Eng. Software 28 (1997) 353–357 (1997).
[12] R. Karch, F. Neumann, M. Neumann, W. Schreiner, Staged growth of optimized arterial model trees, Ann. Biomed. Eng. 28 (2000) 495–511.
[13] I. Hershkovitz, et al., The elusive diploic veins: anthropological and anatomical perspective, Am. J. Phys. Anthropol. 108 (1999) 345–358.
[14] F. Aurenhammert, Power diagrams properties,algorithms and applications, SIAM J. Comput. 16 (1) (1987) 78–96.
[15] J.A. Rhodin, Ultrastructure of mammalian venous capillaries, venules, and small collecting veins, J. Ultrastruct. Res. 25 (1968) 452–500.
[16] H. Hassani-Ardekani, F. Ghalichi, H. Niroomand-Oscuii, M. Farhoudi, M.K. Tarzmani, Comparison of blood flow velocity through the internal carotid artery based on Doppler ultrasound and numerical simulation, Australas. Phys. Eng. S. 35 (2012) 413–422.
[17] N. Filipovic, D. Milasinovic, N. Zdravkovic, D. Böckler, H. von Tengg-Kobligk, Impact of aortic repair based on flow field computer simulation within the thoracic aorta, Comput. Methods Progr. Biomed. 101 (2011) 243–252.
[18] P. Xiaofeng, Hemorheology, University of Eectronic Science and Technology of China Press, Chengdu, 2013, p. 112.
[19] J.N. Oshinski, J.L. Curtin, F. Loth, Mean-average wall shear stress measurements in the common carotid artery, J. Cardiovasc. Magn. Reson. 8 (2006) 717–722.
[20] G. Dong, Q. Lian, L. Yang, W. Mao, S. Liu, C. Xu, Preparation and endothelialization of multi-level vessel-like network in enzymated gelatin scaffolds, JBE 15 (4) (2018) 673–681.
[21] J. Keelan, E.M. Chung, J.P. Hague, Simulated annealing approach to vascular structure with application to the coronary arteries, Royal Society open science 3 (2) (2016) 150431.
[22] W. Schreiner, F. Neumann, M. Neumann, A. End, S.M. Roedler, Anatomical variability and functional ability of vascular trees modeled by constrained constructive optimization, J. Theor. Biol. 187 (2) (1997) 147–158.
[23] J. Yang, Y. Wang, Design of vascular networks: a mathematical model approach, International journal for numerical methods in biomedical engineering 29 (4) (2013) 515–529.
[24] M.E. Andia, M. Henningsson, T. Hussain, A. Phinikaridou, A. Protti, G. Greil, R.M. Botnar, Flow-independent 3D whole-heart vessel wall imaging using an interleaved T2-preparation acquisition, Magn. Reson. Med. 69 (1) (2013) 150–157.
[25] F. Vozzi, F. Bianchi, A. Ahluwalia, C. Domenici, Hydrostatic pressure and shear stress affect endothelin-1 and nitric oxide release by endothelial cells in bioreactors, Biotechnol. J. 9 (1) (2014) 146–154.
[26] R. Attalla, C. Ling, P. Selvaganapathy, Fabrication and characterization of gels with integrated channels using 3D printing with microfluidic nozzle for tissue engineering applications, Biomed. Microdevices 18 (1) (2016) 17.
[27] H.W. Kang, S.J. Lee, I.K. Ko, C. Kengla, J.J. Yoo, A. Atala, A 3D bioprinting system to produce human-scale tissue constructs with structural integrity, Nat. Biotechnol. 34 (3) (2016) 312.
[28] X. Cui, T. Boland, Human microvasculature fabrication using thermal inkjet printing technology, Biomaterials 30 (31) (2009) 6221–6227.
[29] R.N. Pittman, The Circulatory System and Oxygen Transport, (2011).
[30] J. Rouwkema, B.F. Koopman, C.A.V. Blitterswijk, W.J. Dhert, J. Malda, Supply of nutrients to cells in engineered tissues, Biotechnol. Genet. Eng. Rev. 26 (1) (2009)

163–178.
[31] M.C. LeWiS, B.D. Macarthur, J. Malda, G. Pettet, C.P. PleaSe, Heterogeneous proliferation within engineered cartilaginous tissue, the role of oxygen tension, Biotechnol. Bioeng. 91 (5) (2005) 607–615.
[32] M. RadiSic, H. Park, F. Chen, J.E. SalaZar-LaZZaro, Y. Wang, R. DenniS, R. Langer, L.E. Freed, G. VunJak-Novakovic, Biomimetic approach to cardiac tissue engineering, oxygen carriers and channeled scaffolds, Tissue Eng. 12 (8) (2006) 2077–2091.
[33] M.A. SWartZ, M.E. Fleury, Interstitial flow and its effects in soft tissues, Annu. Rev. Biomed. Eng. 9 (2007) 229–256.
[34] G. Helmlinger, R.V. Geiger, S. Schreck, R.M. Nerem, Effects of pulsatile flow on cultured vascular endothelial cell morphology, J. Biomech. Eng. 113 (2) (1991) 123–131.
[35] A.W. Justin, R.A. Brooks, A.E. Markaki, Multi-casting approach for vascular networks in cellularized hydrogels, J. R. Soc. Interface 13 (125) (2016) 20160768.